FINITE ELEMENT CONJUGATE HEAT TRANSFER STRATEGY FOR SELF AND APPLIED MAGNETOPLASMADYNAMIC (MPD) THRUSTERS

K. J. Berry[1]
Department of Mechanical Engineering
[1]Kettering University, Flint, MI

ABSTRACT

Conjugate Heat Transfer (CHT) analysis allows for the simulation of heat transfer between solid and fluid domains by exchanging thermal energy at the solid/fluid interfaces. This exchange is especially important for MPD thruster analysis due to the high temperature plasma (~5000K) heat transfer exchange between the plasma/Cathode and plasma/Anode electrode interfaces. Proper numerical modeling captures both the large electromagnetic current and magnetic field gradients, as well as, the heat transfer thermal gradients, that occur due to large thermal and electrical diffusion coefficient differences at the plasma/solid interface. Although MPD-CHT models are typically not included, attention to such numerical detail yields an improved MPD thruster design process and provides guidance to determine external heat transfer cooling requirements to maintain proper operating parameters. The non-linear coupled finite element formulation herein provides increased stability and presents a computational framework strategy for modeling and analysis of self-field and applied field MPD thrusters considering the highly non-linear, multi-disciplinary, and temperature dependent property requirements of the integrated solid/fluid MPD problem domain. A single numerical modeling design variable (OMEGA) is also introduced that combines experimental and numerical parameters, with reference plasma thermal properties.

Keywords: MPD, CFD, Heat Transfer, Conjugate, Magnetoplasmadynamics, finite elements

NOMENCLATURE

BASE UNITS

m: Meters   A: Amps   V: Volt

N: Newtons   s: Seconds   wb: Weber ($N \ m \ A^{-1}$)

kg: Mass

REFERENCE VARIABLES

U_0 Velocity ($m \ s^{-1}$) T_0 Temperature (K)

P_0 Total Pressure ($N \ m^{-2}$) B_0 Magnetic Field ($wb \ m^{-2}$)

E_0 Electric Field ($V \ m^{-1}$) J_0 Current Density ($A \ m^{-2}$)

σ_0 Conductivity ($A \ V^{-1} \ m^{-1}$) ρ_0 Density ($kg \ m^{-3}$)

μ_0 Permeability Space ($N \ A^{-2}$)

GEOMETRY

R_1 Cathode Radius (m) R_2 Anode Radius (m)

R_3 Throat Radius (m) X_1 Cathode Length (m)

X_2 Anode Length (m) D_0 Flow Depth (m)

A_c Flow Area, $(R_2 - R_1) \bullet D_0 \ (m^2)$

DIMENSIONLESS VARIABLES

$$x^* = \frac{x}{X_2} \qquad \sigma^* = \frac{\sigma}{\sigma_0} \quad U^* = \frac{u}{U_0} \quad T^* = \frac{T}{T_0}$$

$$p^* = \frac{p}{\rho_0 U_0^2} \quad \nabla^* = \frac{1}{X_2} \quad B_0 = \frac{J_0}{\sigma_0 U_0} \quad E_0 = \frac{J_0}{\sigma_0}$$

1. INTRODUCTION

The exothermic chemical propulsion exhaust velocity is governed by the 2nd Law of Thermodynamics which limits the maximum energy available from chemical reactions. The maximum combustion temperature is further limited by combustion chamber materials, and the combustion wall convective heat transfer rate limitation. Nevertheless, these limitations do not govern the use of electric propulsion technology which is driven by magnetoplasmadynamic (MPD) principles.

MPD principles governs the creation of a self-induced magnetic field when an externally applied current $\left(\vec{J}\right)$ passes through an electrical conductor. The applied current furthermore couples with both the "self-induced" magnetic field $\left(\vec{B}\right)$ and an externally "applied" magnetic field $\left(B_0\right)$ resulting in a magnetic force perpendicular to both the current and magnetic fields, i.e., $\vec{F} = \vec{J} \times \vec{B}$. This is known as the Lorentz thrust force, and defines electric MPD propulsion.

Electric MPD propulsion has two thrust mechanisms. The first is the _local_ Ohmic electromagnetic Joule heating of an electrically conductive ionized gas propellant to temperatures higher than those possible via chemical propulsion. The increased thermal enthalpy is thereby converted into kinetic energy through a nozzle as _electrothermal thrust_.

The second thrust mechanism is due to _perpendicular_ interactions between electric and magnetic fields, resulting in _electromagnetic thrust_ in the 'off' direction with no moving parts (i.e., Electromagnetic Lorenz Forces).

The "APPLIED-FIELD" MPD thruster requires the application of both an external electric field via a power source and the integration with an externally applied magnetic field with permanent magnetics encasing the acceleration chamber and generating thrust via the ionized gas propellant.

In contrast, a "SELF-FIELD" MPD thruster is a low-thrust electric propulsion space-system that generates thrust through coupling between an externally applied electric field with a self-induced magnetic field resulting in electromagnetic plasma acceleration.

Although MPD propulsion thrusters are a very promising technology for space exploration, experimental earth-based facilities have pressure restrictions, and have low thrust efficiencies. Furthermore, despite the geometry simplicity, the understanding of MPD performance characteristics is limited by the complex 3D computational physics coupling electromagnetics, fluid dynamics, heat transfer, and geometric parameters. Considering the high experimental cost to determine the impact of many flow and geometric alternatives, numerical methods such as finite elements perhaps is a cost effective strategy to obtain an in-depth understanding of complex MPD processes and using experimental data as a modelling guide.

2. MPD LITERATURE

For 60 years MPD thrusters have undergone extensive experimental study and development [2-4,11-21]. Although these early studies provided insight in MPD experimental operations, detailed theoretical reviews followed with access to improved computational resources. Lapointe [8] used a 2D thermal equilibrium, single fluid MHD code which incorporates classical plasma transport coefficients and Hall effect to predict steady state self-field MPD thruster performance. The code assumes the perfect gas equation of state, a fully ionized plasma gas and does include electrode sheath effects. Lapointe [11]

further refined the calculations through separate calculations of ion and electron temperatures and provided more accuracy for the plasma voltage drop, viscous loss, and thruster efficiency.

Xisto et al., [3] provided a 2D numerical self-field rectangular thruster assuming a completely ionized plasma fluid. However, several phenomena are neglected such as viscosity, thermal conductivity, electrical conductivity, incompressible, electrical sheath, Hall effect and radiation processes. Without including viscous dissipation, it is not possible to capture real momentum and thermal effects such as viscous drag, boundary layer separation, vortex shedding, and recirculation. Xisto et al., [4] further extended model for real gas MHD self-field thrusters with the Spitzer-Harm approximation for the Argon plasma electrical conductivity $\left(\sigma_0\right)$ and included a real gas model for plasma gas density and the specific heat ratio $\left(i.e.\, \gamma = c_p / c_v\right)$. Both models also included a 'slip' wall boundary condition for velocity interfaces, and electrodes were modelled as perfect conductors. The 'slip' condition however limits the model's applicability to relatively high Reynolds number flows.

3. MPD THRUSTER MODEL

Figure 1 shows a typical co-axial MPD thruster. The propulsion system is comprised of a central Cathode surrounded by a concentric Anode. As the propellant enters the chamber it is ionized (via an electric arc between the electrodes) within a few mm of the back plate. The ionization current varies between 4,000-20,000A which results in a plasma ionization temperature between 2,000-10,000K.

The propulsive energy is deposited electrically through an electromagnetic energy conversion mechanism that removes the available energy limitation of chemical thrusters and allows for an expanded range of exhaust velocities that governs the range and duration of space missions due to increased propulsion thrust densities.
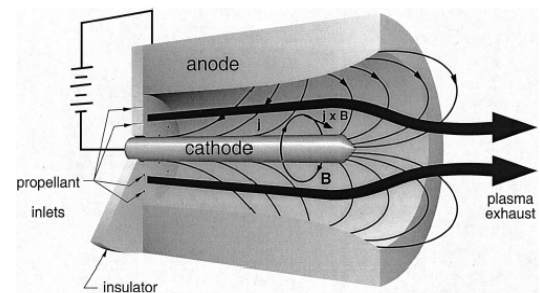

FIGURE 1: MPD THRUSTER

Included herein is the development of a fully coupled non-dimensional time and temperature dependent code for modelling MPD thrusters using the Galerkin Finite Element Method (GFEM). The model includes temperature dependent property models for the fully ionized plasma thermal conductivity, viscosity, electrical conductivity, density, and specific heat plasma properties. The model also incorporates finite element 'natural' gradient boundary conditions to accurately model

induced magnetic field gradients (i.e., currents) as a boundary condition. The author is unaware of natural gradient-based boundary conditions within the literature for MPD simulations.

3.1 MPD Assumptions

The MPD model includes both fluid (Plasma) and Solid (Cathode) finite element subdomains integrated as a single numerical *Conjugate Heat Transfer (CHT)* model. This ensures the simulation captures temperature and magnetic field gradients at the plasma-solid boundary interface. The gas plasma model is a single, quasi-neutral fluid in thermal equilibrium with complete ionization upon entry. Electrical sheath formulation, Hall effects (impacting Ohm's Law), displacement current (impacting Ampere's Law) and radiation processes are neglected. The Argon plasma is considered viscous and a thermally conducting perfect gas.

4. GALERKIN FINITE ELEMENT FORMULAION

Herein is the development of a coupled time variant and temperature dependent code for modelling MPD thrusters using the Galerkin Finite Element Method (GFEM). The model includes temperature dependent properties and magnetic field gradient boundary conditions to accurately model the induced magnetic field density and heat transfer rates throughout the solid/plasma computational domain.

The GFEM for numerical modeling results in an equation system of the form [6]:

$$\int_{\Omega^{(e)}} [A(\phi^{(e)}) - f^{(e)}]N_i^{(e)} d\Omega = 0, \quad i = 1, 2, ...r \quad (1)$$

Where (e) is over the range for a discrete element and "r" is the unknow parameters over element (e) and $\phi^{(e)}$ represented as:

$$\phi^{(e)} = \left[N^{(e)} \right]\{\phi\}^{(e)}$$

where :

[N] = shape function matrix

$\text{f}^{(e)}$ = forcing function defined over element (e)

(2)

The GFEM results in the use of Gauss's theorem for integration by parts over each finite element volume Ω and results for 2nd order derivatives are of the form:

$$\int_\Omega N^T (\nabla \bullet \nabla \phi) d\Omega = \int_\Gamma N^T (\nabla \phi \bullet \hat{n}) d\Gamma - \int_\Omega \nabla \phi \bullet \nabla N^T d\Omega = 0 \quad (3)$$

Equation 3 has surface integral Γ representing natural **GRADIENT-BASED BOUNDARY CONDITIONS** and is advantageous for modelling of MHD phenomena requiring magnetic field gradients as boundary conditions.

The magnetic flux and current density gradient-based boundary conditions are [5]:

$$\hat{n} \bullet \vec{J} = \hat{n} \bullet \nabla \times \frac{1}{\mu_0} \vec{B} = 0 \rightarrow \text{ INSULATOR}$$

$$(4)$$

$$\hat{n} \times \vec{J} = \hat{n} \times (\nabla \times \frac{1}{\mu_0} \vec{B}) = 0 \rightarrow \text{CONDUCTOR}$$

and is accommodated by the GFEM and is assembled within the finite element stiffness matrix of the form $[K]\{\phi^{(e)}\} = \{f^{(e)}\}$.

4.1 Source Term Modelling

Past experimental work indicated possible issues with gradient driven MPD thruster instabilities [21]. Numerical MPD thruster modelling requires the integration of fluid mechanics, heat transfer, and electromagnetics through coupling of explicit source terms from a prior iteration based upon the gradient of primary solution variable such as the magnetic field density, i.e., $\vec{B}$.

However, gradient source terms can fluctuate greatly, from iteration to the next, depending upon geometry gradients (i.e., corners), temperature dependent properties, and flow conditions. Due to time scale differences between the Navier-Stokes and Maxwells domain equations, the current density distribution can be large and rapidly fluctuating; this will strain the Lorentz body force and Joule Ohmic heating terms and resulting in elevated source vectors that drive the fluid system equations to become very large and 'stiff [20]. Likewise, high electrical conductivity gradients will increase the current density and subsequently the source coupling vector and causing a 'stiff' computational domain. This can also be an issue with integrated CHT solutions that include both "solid—Cathode" and a "fluid-plasma" interface due to large conductivity differences.

A computational advantage of the GFEM is the inherent ability to assemble gradient based elemental force components into the local element stiffness matrix. The resulting equation set are recast into a strong conservative form allowing the coupling of Navier-Stokes, Maxwell, and Conservation of Energy equations, and removes the appearance of right-hand side explicit source terms while retaining an exact coupling to the full multi-physics domain equations *i.e.*, $[K]\{\phi^{(e)}\} = \{0\}$. This approach relieves '*numerical stiffness*' (since no source terms are present), and results in improved stability. The strategy of replacing *source coupling* with *flux coupling* has been noted by several researchers [28-30], but to the authors' knowledge the only implementation has been for a finite volume implicit Euler based Rieman solver formulation [20].

5. MAXWELL MAGNETIC INDUCTION

MHD governs the interaction between magnetic fields and the interaction with an electrically conducting fluid. The magnetic induction equation defines the *induced* magnetic field governed by Ampere's Law. The non-dimensional Maxwell electromagnetic equations ignoring electric point charges are:

$(a)\ \nabla^* \bullet \vec{B}^* = 0$

$(b)\ \dfrac{1}{Rm}\nabla^* \times \vec{B}^* = \vec{J}^*$ (Ampere's Law)

$(c)\ \nabla^* \bullet \vec{E}^* = 0$ (Gauss's Law) $\qquad$ (5)

$(d)\ \nabla^* \times \vec{E}^* = -St\dfrac{\partial \vec{B}^*}{\partial t^*}$ (Faraday's Law)

$(e)\ \vec{J}^* = \sigma^*(T^*)\left[\vec{E}^* + \vec{U}^* \times \vec{B}^*\right]$ (Ohm's Law)

The Curl $(\nabla\times)$ of 5b and incorporating 5d and 5e provides the 3D Maxwell Induction Equation of the form [1]:

$$\sigma^*\left[St\left(\dfrac{\partial B^*}{\partial t^*}\right) + (\vec{U}^* \bullet \nabla)\vec{B}^* + \nabla^*(\nabla^* \bullet \vec{B}^*)\right] =$$

$$\dfrac{\nabla^2 \vec{B}^*}{Rm} + \nabla\sigma^* \times \vec{E}^* + \left(\nabla\sigma^*\right)\times\left(\vec{U}^* \times \vec{B}^*\right) + \qquad (6)$$

$$\sigma^*\left(-\vec{B}^*(\nabla^* \bullet \vec{U}^*) + (\vec{B}^* \bullet \nabla^*)\vec{U}^*\right)$$

with dimensionless variables defined as:

$$St \equiv \text{Strouhal \#} = \dfrac{X_2/U_0}{\Delta t_0} = f_m\dfrac{X_2}{U_0}$$

$$f_m \equiv \text{Mag. Vortex Freq.} = \dfrac{1}{\Delta t_0}, \mu_0 \equiv \text{Permeability} \qquad (7)$$

$$Rm \equiv \text{Magnetic Reynolds} = \mu_0 X_2 \sigma_0 U_0$$

$$= \dfrac{\text{Magnetic Convection}}{\text{Magnetic Diffusion}}$$

The divergence of the velocity field $\nabla^* \bullet \vec{U}^*$ allows the coupling of the magnetic and compressible velocity flow fields, $\nabla\sigma^*$ is the electrical conductivity gradient, and terms $\nabla^*(\nabla^* \bullet \vec{B}^*)$ and $(\vec{B}^* \bullet \nabla^*)\vec{U}^*$ ensures 3D divergence free flow. As stated previously, gradient coupling terms are not an issue and are assembled directly into the GFEM finite element stiffness matrix.

6. NAVIER-STOKES MHD COUPLING

MHD electromagnetics and Navier-Stokes are coupled through the Maxwell Induction Equation and the applied current. The conservation of mass for compressible flow is expressed as:

$$St\dfrac{\partial \rho^*}{\partial t^*} + \nabla^* \bullet (\rho^* \vec{U}^*) = 0 \qquad (8)$$

The conservation of momentum for compressible flow is expressed as:

$$St\dfrac{\partial(\rho^* \vec{U}^*)}{\partial t^*} + \nabla^* \bullet \left(\rho^* \vec{U}^* \vec{U}^* + \hat{p}^*[I]\right) - \dfrac{1}{Re}\nabla^* \bullet \tau_{visc}^* \qquad (9)$$

$$= \dfrac{\Psi}{Rm}\nabla^* \times \vec{B}^* \times \vec{B}^*$$

With dimensionless variables defined as:

$$\Psi \equiv \dfrac{\text{Magnetic Force}}{\text{Inertia Force}} = \dfrac{\text{Ha}^2}{\text{Re}}$$

$$\text{Ha}^2 \equiv \dfrac{\text{Magnetic Force}}{\text{Viscous Force}} = \dfrac{B_0^2 \sigma_0 X_2^2}{\mu_{fluid}} = \text{Hartman \#} \qquad (10)$$

$$\text{Re} \equiv \dfrac{\text{Intertia Force}}{\text{Viscous Force}} = \dfrac{\rho_0 U_0 L_c}{\mu_{fluid}} = \text{Reynolds \#}$$

The constitutive relations are defined as:

$$\hat{p}^* = p^* + \dfrac{\vec{B}^* \bullet \vec{B}^*}{2\mu_0}\dfrac{B_0^2}{\rho_0 U_0^2 / X_2}$$

$$\tau_{visc}^* = -\left(\dfrac{2}{3}\mu_{fluid}^*(T^*)\nabla^* \bullet \vec{U}^*\right)[I] + \qquad (11)$$

$$\mu_{fluid}^*(T^*)\left[\nabla^* \vec{U}^* + \left(\nabla^* \vec{U}^*\right)^T\right]$$

$$\mu_{fluid}^* \equiv \text{Fluid Viscosity}$$

where $\hat{p}^*$ is the total hydro static and magnetic pressure, $[I]$ is the identity matrix, and τ_{visc}^* is the viscous stress tensor for compressible Newtonian flow. The momentum magnetic force gradient term $\dfrac{\Psi}{Rm}\nabla^* \times \vec{B}^* \times \vec{B}^*$ allows coupling to the magnetic induction equation and is assembled within the finite element stiffness matrix. The conservation of energy equation is expressed as:

$$St\dfrac{\partial\left(\rho^* E_t^*\right)}{\partial t^*} + \nabla^* \bullet \left(\rho^* E_t^* + \hat{p}^*\right)\vec{U}^* -$$

$$\dfrac{1}{Pe}\nabla^* \bullet \left(\dfrac{k_{th}^*}{\rho^* c_v^*}\nabla^*\left(\rho^* E_t^*\right)\right) =$$

$$\dfrac{\mu_{fluid}^* Ec}{Re}\nabla^* \bullet (\tau_{visc}^* \bullet \vec{U}^*) + \qquad (12)$$

$$\dfrac{\Psi Ec}{Rm}\left(\vec{E}^* \bullet \nabla^* \times \vec{B}^* + \left(\nabla^* \times \vec{B}^* x \vec{B}^*\right) \bullet \vec{U}^*\right)$$

With dimensionless variables defined as:

$$Ec \equiv \text{Eckert \#} = \frac{U_0^2}{c_{p0}T_0} \equiv \frac{\text{Advective Mass Transport}}{\text{Heat Diffusion Potential}}$$

$$Pe \equiv \text{Peclet \#} = \text{Re} \bullet \text{Pr} \qquad (13)$$

$$Pr \equiv \text{Prandtl \#} = \frac{\mu_{fluid}c_p}{k_{th}}$$

Where $\left(\nabla^* \times \vec{B}^* x \vec{B}^*\right) \bullet \vec{U}^*$ is the work done by the magnetic thrust force on the plasma and is coupled through the magnetic induction and velocity flow field. The magnetic thermal load term $\left(\vec{E}^* \bullet \nabla^* \times \vec{B}^*\right)$ is the current resistivity work and couples the total magnetic energy to the magnetic induction equation. Both gradient based terms are assembled within the finite element stiffness matrix.

$\dot{E}_t[J/kg]$ is the total magnetic plasma energy for a perfect gas expressed as:

$$\rho^* \dot{E}_t^* = \rho^* T^* + \frac{\rho^* U^{2^*} E_c \gamma}{2} + \frac{B_0^2}{2\mu_0} \frac{1}{\rho_0 c_{v0} T_0} \qquad (14)$$

The temperature is derived from the equation of state of the form:

$$T^* = \frac{\rho^* \dot{E}_t^* - \frac{\rho^* U^{2^*} E_c \gamma}{2} - \frac{B_0^2}{2\mu_0} \frac{1}{\rho_0 c_{v0} T_0}}{\rho^*} \qquad (15)$$

7. CATHODE CHT MODEL

The Cathode CHT model includes both plasma and solid finite element computational domains with a common boundary. To ensure continuity of electric and magnetic fields, as well as temperature and heat flux at the plasma-solid interface, the temperature, thermal conductivity, and electrical conductivity property value are common to both the plasma and solid Cathode.

Within the solid Cathode domain, a 2D property gradient function was developed based upon the Cathode internal geometry coordinates. The property value (P(u)) is defined according to the following parametric cubic function for both the axial and radial dimensions:

$$0 \leq r \leq R_1, \text{ and, } 0 \leq x \leq X_1$$
$$0 \leq u \leq 1 \qquad (16)$$
$$P(u(r)) = A_0 + B_0 u + C_0 u^2 + D_0 u^3$$

Where the eight (8) constants are determined from the following constraints in both coordinate directions:

$$P_{u=0} = P_{cathode}$$
$$\frac{dP}{du}_{u=0} = 0$$
$$P_{u=1} = P_{Plasma} \qquad (17)$$
$$\frac{dP}{du}_{u=1} = 0$$

The result provides at each internal nodal point two functions in terms of coordinates "X", and "Y". The effective property at each nodal point is defined as:

$$\|P_{eff}\| = \sqrt{\{P_x(u)\}^2 + \{P_y(u)\}^2} \qquad (18)$$

The prevailing thought is that at the molecular level the diffusion coefficient, thermal conductivity as an example, <u>must</u> adjust from the "solid" property value to the "plasma" property value as approaching the Cathode/plasma interface. At the interface an effective modeling strategy requires a unique property value at each computational nodal location.

The above strategy allows the property change to approach the Cathode boundary gradually rather than a "step" change at the plasma/Cathode boundary interface. This property gradient strategy is executed after each iteration and allows for smooth and consistent primary variable solutions across the interface boundary and throughout the solid computational domain. The strategy ensures heat flux and magnetic flux continuity at the interface expressed as:

$$\left(\vec{q} \bullet \hat{n}\right)_{cathode} = \left(\vec{q} \bullet \hat{n}\right)_{plasma}$$
$$\left(\vec{J} \bullet \hat{n}\right)_{cathode} = \left(\vec{J} \bullet \hat{n}\right)_{plasma} \qquad (19)$$

The coupled finite element algorithm solves the Maxwell electromagnetic equations for electric current and magnetic field density, and the Navier-Stokes conservation equations for velocity, pressure, and temperature fields. This formulation is presented herein as the VPTB primitive variable method and provides a coupled plasma/solid direct solution rather than a typical segregated iterative approach.

Figure 2 shows a typical result for the effective Cathode property distribution. The darker color near the base represents the larger core Cathode property value, and the lighter color near the Cathode tip represents the smaller property value approaching the Cathode/plasma interface.

Table 1 shows the property comparison between a typical ARGON GAS plasma, and a TUNGSTEN Cathode material, as well as the ratio between the Cathode and Argon property values. Note the rather large ratio for thermal and electrical conductivity and drives the consideration of property gradient solid domain

models to improve accuracy and computational efficiency. This is of interest if anticipating large current/voltage, and thermal gradients near the interface and throughout the solid domain.
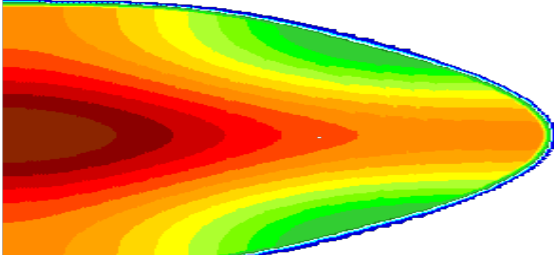

FIGURE 2: EFFECTIVE CATHODE PROPERTY DISTRIBUTION

The author is unaware of other solid property gradient efforts within the literature.

PROP	TUNGSTEN	ARGON	RATIO
DENSITY kg/m^3	0.01563	1.8X10^{-4}	87
THERMAL COND W/m-K	110	0.2	550
CP J/kg-K	200	1000	0.001
ELECTRICAL COND A/V-m	2.4X10^6	1000	2400

TABLE 1: ARGON/CATHODE MATERIALS RATIO

8. FINITE ELEMENT FORMULATION

To support the general finite element practitioner, the coupled 2D MPD plasma variables are axial current density $(J_z^*(z,y,t))$ and lateral current density $(J_y^*(z,y,t))$ (Equation 5b), magnetic field density $(B_z^*(z,y,t))$ (Equation 6), pressure $(P^*(z,y,t))$ (Equation 8), velocity $(\vec{V}^*(z,y,t))$ (Equation 9), and total magnetic energy $(E_t^*(z,y,t))$ (Equation 12). The nine-node bi-quadrilateral finite element represents MPD variables at each of the nine nodes, except the pressure is computed at four (4) corner nodes only. The coupled global finite element stiffness matrix Equation 20 below is of size [68x68] where each of the primary variables sub matrices are of size [9x9] as they are computed at each of the nine nodes, except for sub-matrix [K$_{up}$] that is of size 9x4, [K$_{pu}$] that is of size 4x9, and sub-matrix [K$_{pp}$] that is of size 4x4 as pressure is only computed at the 4 corner nodes. Hubener [6] provides more detail regarding the mixed-variable u-v-p finite element formulation for velocity and pressure adopted here.

Numerical integration of sub-matrices above is beyond the scope herein but is presented in other references, i.e., [6,7,24], and C-based CHAOS software is available through communications with the author.

$$[K_{68 \times 68}] = \begin{bmatrix} K_{uu} & K_{uv} & K_{up} & K_{uJx} & K_{uJy} & K_{uB} & K_{uE} \\ & K_{vv} & & & & & \\ & & K_{pp} & & & & \\ & & & K_{J_{zz}} & & & \\ & & & & K_{J_{yy}} & & \\ & & & & & K_{BB} & \\ K_{Eu} & K_{Ev} & K_{Ep} & K_{EJx} & K_{EJy} & K_{EB} & K_{EE} \end{bmatrix} \quad (20)$$

Figure 3 shows the 9-node Bi-Quadratic parametric finite element used to represent coupled MPD variables.
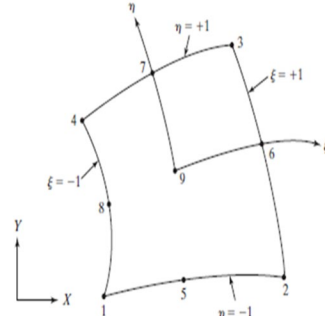

FIGURE 3: 9-NODE BI-QUARDATIC ELEMENT

8.1 Temporal Discretization

The time varying and coupled finite element MPD differential equations are expressed generally as [6]:

$$[C]\{\dot{\phi}\}_\theta + [K]\{\phi\}_\theta = \{R(t_\theta)\}$$
$$t_\theta = t_n + \theta\Delta t, where:$$
$$0 \le \theta \le 1 \quad (21)$$
$$\phi^T = \{ u \quad v \quad P \quad J_z \quad J_y \quad B_z \quad E_t \}$$

A general set of recursive relations are defined by introducing:

$$\{\dot{\phi}\}_\theta = \frac{\phi_{n+1} - \phi_n}{\Delta t}$$
$$\{\phi\}_\theta = (1-\theta)\{\phi\}_n + \theta\{\phi\}_{n+1} \quad (22)$$
$$\{R(t_\theta)\}_\theta = (1-\theta)\{R\}_n + \theta\{R\}_{n+1}$$

For a given θ combining equations 21 and 22 provide a recurrence relation for nodal values at the end of a time step of the form:

$$[\overline{K}]\{\phi\}_{n+1} = \{\overline{R}\}_{n+1}\,; where$$

$$[\overline{K}] = \theta[K] + \frac{1}{\Delta t}[C]$$

$$\{\overline{R}\}_{n+1} = \left[-(1-\theta)[K] + \frac{1}{\Delta t}[C]\right]\{\phi\}_n \qquad (23)$$

$$+ (1-\theta)\{R\}_n + \theta\{R\}_{n+1}$$

Where $\{\phi\}_{n+1}$ are unknowns for time step n+1. For the finite element work herein $\theta = 0$, which is defined as the forward difference or Euler method for time discretization.

9. EXPERIMENTAL DRIVEN NUMERICAL VARIABLES

Non-dimensional formulations provide valuable insight into dimensionless parametric groups that control the system dynamics and response. The MPD core dimensionless groups are the viscous and magnetic Reynolds #, the Eckert #, and the Hartman #. However, these numerical parametric groups are NOT random and must be related to experimental operational parameters for real systems. The experimental parameters are mass flow rate (kg-s^{-1}), current density (A-m^{-2}), and Reference Temperature (K) along with geometric parameters of Cathode Length (X_1) and radius (R_1), and Anode Radius (R_2).

Another reality of dimensionless parametric groups is that different combinations of individual parameters within the group will provide the same computational result, that often is non-intuitive. Ideally the goal is to define a "*single*" non dimensional group as the primary independent control variable, while also linked to experimental and numerical control variables.

Toward this goal, define the geometric scaling factor as the Anode Length, X_2, and reconsidering the non-dimensionalization of the conservation of momentum equation right-hand-side forcing term (9):

$$F_m^* = J \times B\left(\frac{X_2}{\rho_0 U_0^2}\right) = \frac{1}{\mu_0}\nabla \times B \times B\left(\frac{X_2}{\rho_0 U_0^2}\right)$$

$$= \frac{\omega}{Rm}\nabla^* \times B^* \times B^* \qquad (24)$$

With ω (*OMEGA*) and magnetic reference velocity defined as:

$$\omega(J_0, \rho_0, \sigma_0)\left[\frac{m^2}{s^3}\right] = \frac{J_0^2}{\rho_0 \sigma_0} \qquad (25)$$

$$U_0(\omega, X_2)[\frac{m}{s}] = (\omega X_2)^{\frac{1}{3}} \qquad (26)$$

ω (*OMEGA*) is linked to the experimental reference current density (J_0), reference temperature (T_0), plasma electrical conductivity (σ_0), and the magnetic reference velocity is linked to ω and the experimental Anode length (X_2).

From the experimental geometry and mass flow rate, ω provides a single relationship between experimental and plasma properties and controls the following modeling parameters:

$$Ma\# = \frac{U_0}{\sqrt{kRT_0}}$$

$$Ec \equiv \text{Eckert}\# = \frac{U_0^2}{cp_0 T_0}$$

$$A_c[m^2] = \frac{\dot{m}}{\rho_0 U_0} \qquad (27)$$

$$Re = \frac{\rho_0 U_0 X_1}{\mu_f}$$

Similarly, the Magnetic Reynolds # (Rm) as an input parameter defines the Cathode Length, X_1 (or vice-versa).:

$$Rm = \mu_0 \sigma_0 U_0 X_1, or:$$

$$X_1 = \frac{Rm}{\mu_0 \sigma_0 U_0} \qquad (28)$$

From Equations 24-28, the numerical analysis is driven by experimental parameters of mass flow rate, reference current density, reference temperature and properties, and reference experimental geometry.

Substitution for the conservation of energy equation right-hand-side forcing term becomes:

$$\frac{E_c(U_0(\omega))}{Rm}\left(\vec{E}^* \bullet \nabla^* \times \vec{B}^* + \left(\nabla^* \times \vec{B}^* x \vec{B}^*\right)\bullet \vec{U}^*\right) \qquad (29)$$

As previously stated, these "gradient-based" forcing terms are included with the global finite element stiffness matrix. Note that for a fixed geometry, mass flow rate, reference temperature and plasma properties, the experimental and numerical analysis is controlled by a "single" variable, ω.

9.1 Argon Gas Plasma Properties

Temperature dependent thermal property data is critical for all MPD numerical analysis, although challenging to retrieve from the literature. Argon is the selected gas plasma for the study herein and is perhaps the most common. Berry [1] modelled Argon plasma property data with a series of piecewise continuous parametric cubic curves per Equation 29 for **density**, **viscosity**, **specific heat**, **thermal conductivity, and electrical conductivity**,

$$P(u) = A_0 + B_o u + C_0 u^2 + D_o u^3; 0 \le u \le 1.0 \qquad (30)$$

based upon published experimental data [22,23] over temperature range: 2500-30,000K. See [1] for complete coefficient values.

For example, Figure 4 shows the Argon plasma specific heat variation vs. Temperature, and it is important to observe the inflection points impacting the conversion increase or decrease of thermal energy to kinetic convective acceleration or thrust. Complete temperature dependent ARGON property modelling parameters needed for MPD heat transfer simulation and design optimization are provided.
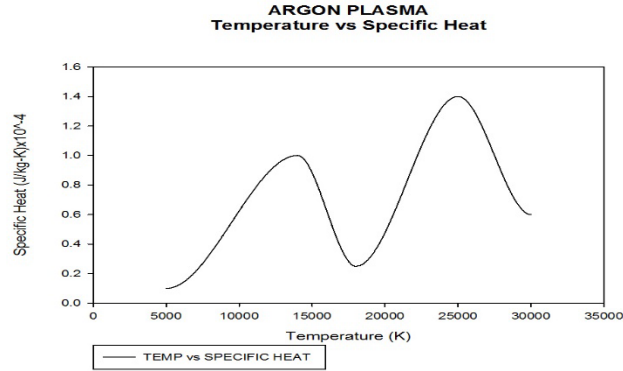

ARGON PLASMA
Temperature vs Specific Heat

FIGURE 4: SPECIFIC HEAT TEMPERATURE MODEL

10. NUMERICAL MODEL

MPD thruster numerical analysis including heat transfer represents one of the more challenging domains for computational fluid dynamics, and especially when attempting to compare with other computational models or experimental data. Due to domain non-linearities, gradient based forcing functions and boundary conditions, and temperature dependent thermal properties, computational formulations often differ with terms neglected or included simplification in wall conditions (i.e., slip vs no-slip), incomplete thermal properties, overlooking viscous/thermal diffusion, and/or inadequate geometry information to accurately replicate and to compare the analysis.

To showcase the validity of GFEM algorithm we will compare results presented by Chelem & Groll [24] to model the Villani-H Thruster due the coaxial geometry simplicity. The code used was a "finite volume" discretization with the well-known PISO algorithm for magnetic pressure correction which is a density-based method. The code solves equations in a segregated approach, meaning that for each system of governing equations, separate matrix domain equations are solved iteratively. The computational domain was subdivided into 1,500,000 cells.

The MPD geometry characteristics are shown in Figure 5 with geometric input parameters of X1: Cathode Length, X2: Anode Length, X3: Domain Exit Boundary (not provided), R1: Cathode Radius, and R2: Anode Radius. Operating parameters are mass flow rate: 6 g/s, discharge current, and ionization temperature (not provided).

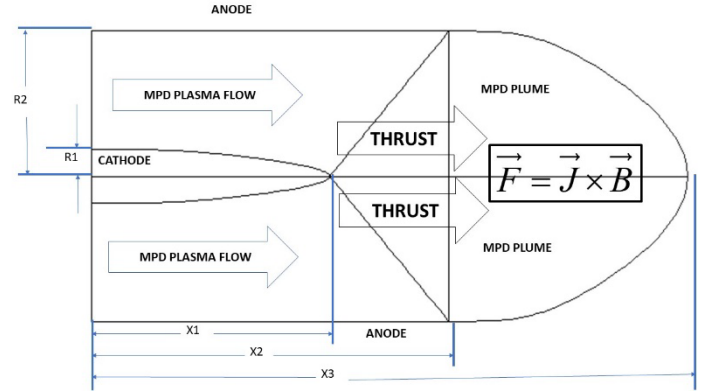The modeling parameters used herein for comparison are:

FIGURE 5: MPD THRUSTER

$$\dot{m} = 0.006\frac{kg}{s}, \quad Temp = 4,000K$$

$$Rm = 0.1077, \quad Ec = 0.1, \quad Re = 230$$

$$R_1(\text{Cathode Radius}) = 0.0095m$$

$$\frac{X_1(\text{Cathode Length})}{R_1(\text{Cathode Radius})} = 14, \tag{31}$$

$$\frac{X_2(\text{Anode Length})}{R_1(\text{Cathode Radius})} = 21$$

$$\frac{X_3(\text{Anode+Plume Length})}{R_1(\text{Cathode Radius})} = 24,$$

$$\frac{X_1(\text{Cathode Length})}{R_2(\text{Anode Radius})} = 5.2$$

The applied discharge current for comparison is:

$$\frac{I^2}{\dot{m}}\left[\frac{A^2\ s}{kg}\right] = 2\times10^9 - 1\times10^{10} \tag{32}$$

The assumed ionization temperature of 4,000k results in the following plasma properties [1] shown in Table 2:

TABLE 2: ARGON PLASMA PROPERTIES: 4,000K

PROP.	VALUE
cp	1358 J/kg-K
kxx	0.19 J/kg-K
pr	0.685
visc	9.8E-5 Pa-s
Sigma	583 A-m/V
Dens	1.53E-4 kg/m3
cp/cv	1.4

The specific modeling geometric and solution variables are provided in Table 3.

TABLE 3: MODELING/SOLUTION VARIABLES

VARIABLE	VALUE
Equations	141,307
Elements	5,600
Nodes	19,840
Constraints	141,307
CPU Sec/Itt.	492

10.1 The OMEGA FACTOR and Magnetic Thrust

ω (Equation 25) provides a single dimensionless modeling parameter based upon geometry, flow, thermal properties, and experimental current density data. Table 4 provides the ω values for the comparison simulation.

TABLE 4. OMEGA SIMULATION DATA

CURRENT A^2-s/kg	OMEGA
2E+9	0.90
4E+9	1.80
6E+9	2.70
8E+9	3.60

The magnetic thrust (T_m) is calculated for each iteration as:

$$T_m[N] = \forall_0 [m^3][J_0 B_0] \left[\frac{N}{m^3} \right] \sum_e \left\{ \int_V J_y^* B_z^* dV^* \right\} \quad (33)$$

$$\forall_0 \equiv \text{current carying volume}$$

Where the integral applies for each current carrying fluid element within the domain.

10.2 Boundary Conditions

The no-slip wall condition is applied for <u>all</u> solid/plasma interfaces, and all velocity components within the solid Cathode is set to zero. The dimensionless temperature T^* is set as 1.0 at plasma inlet, and for the Cathode and Anode boundary surfaces.

Regarding the magnetic field boundary conditions, the Cathode and Anode boundary surface is assumed to be a perfect conductor (Equation 4), and the lateral current (J_y) is applied as a gradient boundary condition at the plasma duct inlet in the form:

$$J_y^* = \pm 1 = \frac{1}{Rm} \int_S \frac{\partial B_z}{\partial x} d\Gamma \quad (34)$$

The author believes that applying current boundary conditions for plasma inlet flows is more appropriate since the resultant current flow is caused by magnetic field "gradients", rather than the absolute value of the magnetic field. Once again, applying gradient based boundary conditions is inherent to the finite element method whereas with other numerical methods, such as finite difference and finite volumes, this capability is not possible.

11. COMPARISON RESULTS

Figure 6 shows a plot of Current $(A^{-2} s\ kg^{-1})$ vs Thrust (N) and compares the author's model with 5,600 9-node coupled parametric 'finite element' direct matrix solution algorithm with the 1,500,00-cell 'finite volume' segregated approach, Chelem [26], and also compared with the standard Macker (1955) electromagnetic coaxial self-field thrust model of the form:

$$F_{Mac\ker} = \frac{\mu_0}{4\pi} I^2 (\ln \left[\frac{r_{anode}}{r_{cathode}} \right] + A) \quad (35)$$

Where the dimensionless constant is taken as A=0 (without justification).
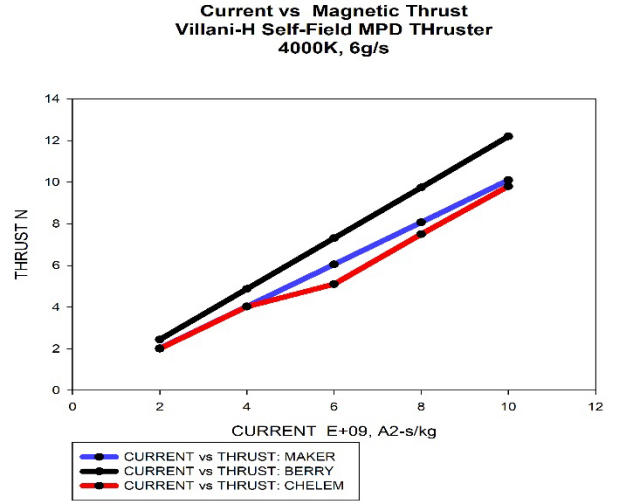

FIGURE 6. CURRENT VS THRUST: VILLANI-H MPD

Although results are similar with same trends, differences may be expected due to:

- Unable to determine reference temperature for plasma properties which impacts thrust.
- Uncertain if an exit plum was included downstream, herein exit plum was 2X times Cathode length.
- The plasma inlet boundary condition is different which also influences computational results. As opposed to a dimensionless current density gradient boundary condition (∇B) used herein (Equation 34), the primary variable B_z is applied as a boundary condition of the form [26]:

$$B_0 = \frac{\mu_0 I}{2\pi r} \quad (36)$$

$$r_{cathode} \leq r \leq r_{anode}$$

Where "I" is the total discharge current and at the inlet the magnetic field boundary condition is calculated as a function of the current.

Figure 7 below shows the *CONTOUR FILL* plot for the dimensionless magnetic field, $B_z(x,y)$ (not-to-scale). Note the continuous magnetic field lines at the Cathode/plasma interface, as well as the continuity throughout the Cathode solid elements. Lines of constant magnetic field also indicate the path of electric current flow.
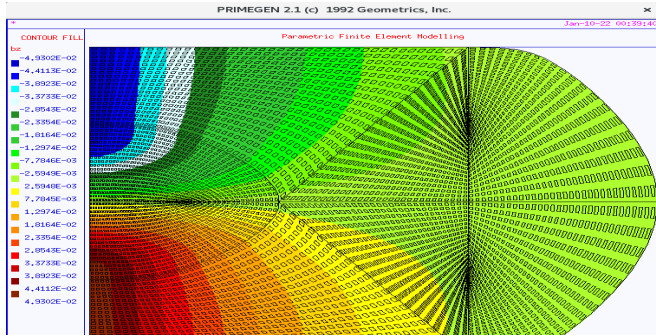

FIGURE 7: MAGNETIC FIELD DENSITY CONTOURS

The ability to model both the plasma fluid elements and the solid Cathode within a single computational domain relative to determining plasma voltage potential drop from Anode to Cathode expressed as:

$$\Delta V_{AB} = -\int_A^B E_y dy \qquad (37)$$

Figure 8 shows the variation of the Anode/Cathode voltage drop as a function of the Cathode length to Cathode radius (X1/R1) with a magnetic Reynolds number of 0.6 (Rm). Note that:

1) The voltage potential increases with increased Cathode length,

2) Due the assumption of a perfectly conducting Anode electrode (zero resistance) the voltage potential is constant over the core of the plasma fluid inlet and increases as approaching the Anode, and,

3) The voltage potential decreases and approaches zero at the centerline as approaching the Cathode boundary as the Cathode is considered as a "real" material and is not an ideal perfect conductor. This behavior is correct as the Cathode centerline voltage potential must be zero.

The non-inclusion of an integrated Cathode/plasma domain results in an ad hoc approach of adding 20V to the result of equation 36 [26,30]. This is advantage of an integrated fluid/solid model in that being able to capture real gradients at the interface.
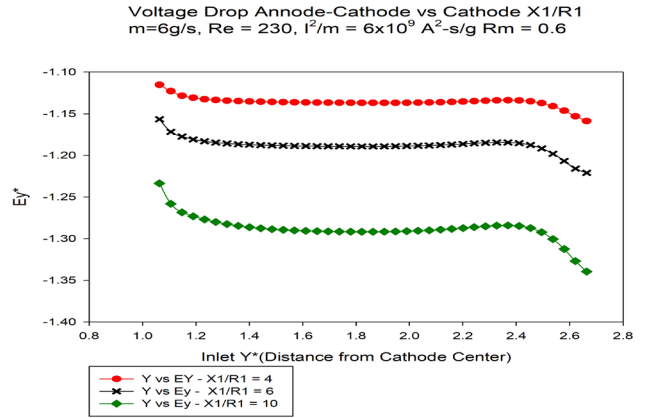

FIGURE 8: Cathode Voltage Drop vs. X1/R1

Figure 9 shows the result of equation 37 for the Anode/Cathode voltage drop vs X1/R1. The voltage drop ranges from 19V to 22V based upon the Cathode length/radius (X1/R1: 4-10).
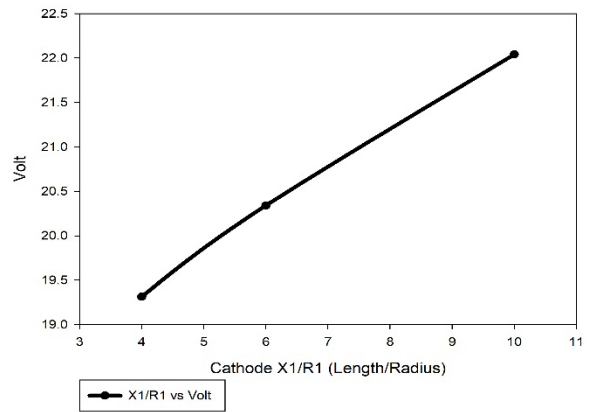

FIGURE 9 : ANODE/CATHODE VOLTAGE DROP

These voltages compare well to Mayigue & Groll [9] at 25.27V, Sankaran of 30.83V [30], and Ahangar of 24.67V [31], considering the unknown magnetic Reynolds number which is an important modeling parameter.

11.1 Numerical Convergence

The stability of any numerical non-linear algorithm is based upon the convergence criteria and the rate of convergence. Herein we use the Global Residual Norm expressed as:

$$\beta = \frac{\max \left| \phi^{i+1} - \phi^i \right|}{\sum_{i=1}^n \phi^i} < 1x10^{-4} \qquad (38)$$

Where ϕ is the variable value at iteration "i", β is defined as the Global Residual Norm (GRN) for all computational variables and "n" is the number of global variables. Figure 10 shows the GRN decay for two cases of Re = 1000, and 3000 with an applied current of 6,000 Amps and mass flow rate of 6g/s. Note the robust convergence for this geometry and operating conditions. A grid independence study was also completed by increasing the
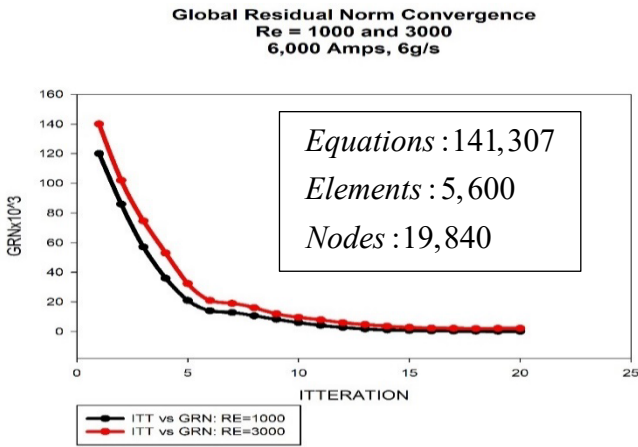

$$Equations: 141,307$$
$$Elements: 5,600$$
$$Nodes: 19,840$$

FIGURE 10: RESIDUAL NORM VS. ITTERATION

number elements by 30% and 60% without alterations in the numerical results.

12. FINITE ELEMENT DESIGN SIMULATION

Finite Element Modeling (FEM) has the primary advantage for engineers in providing data to compare design alternatives. This is especially useful for MPD design optimization studies due to the many different design and operating variables. The dimensionless MPD formulation provides insight to parameters that control and govern overall performance. Here we provide data with a fixed mass flow rate (6 g/s), Reynolds No. (230), and ionization temperature (4,000K). Figure 11 shows the Magnetic Thrust (equation 33) variation as a function of Rm (0.2-0.8) and Cathode length/radius ratio (4-14). Observe that for any fixed value of Rm the magnetic thrust variation is slightly quadratic with increasing Cathode length with a fixed Cathode radius.
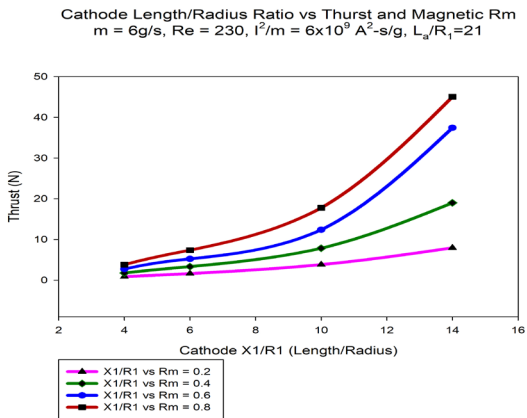

FIGURE 11: THRUST VS MAGNETIC REYNOLDS NO.

Note the strong importance of Rm (magnetic convection/magnetic diffusion) relative to operating performance and thrust generation. For any fixed value of Cathode/radius length ratio, the magnetic thrust various approximately linearly with Rm.

The magnetic flow efficiency based upon the magnetic thrust (33) is defined as:

$$\eta_m = \frac{\dot{P}_{output}}{\dot{P}_{input}} = \frac{T_m[N] \bullet \bar{U}_m \left[\dfrac{m}{s} \right]}{E_0 \left[\dfrac{V}{m} \right] \bullet I_0 [Amps] \bullet (R_{anode} - R_{cathode})[m]}$$

$$\bar{U}_m = \frac{\displaystyle\int_0^{R_{anode}} u_{exit} \rho_{exit} d\Gamma}{\displaystyle\int_0^{R_{anode}} \rho_{exit} d\Gamma} \left[\frac{m}{s} \right] \equiv \text{mean exit velocity} \qquad (39)$$

$$E_0 = \frac{J_0}{\sigma_0} \left[\frac{V}{m} \right] \equiv \text{reference voltage per unit length}$$

The magnetic flow efficiency is a measure of the magnetic conversion efficiency from the input electrical power to the production of magnetic thrust. It is not the total thrust due to the increase of the plasma exit momentum which is the sum of the magnetic conversion thrust and the thermal conversion thrust.

Figure 12 shows the magnetic flow efficiency vs. Rm and Cathode length/radius ratio. Note that flow efficiency increases slightly in a quadratic manner with both the Cathode length and Rm. Depending upon the value of Rm and the Cathode length ratio, the magnetic flow efficiency is shown as high as 30%.
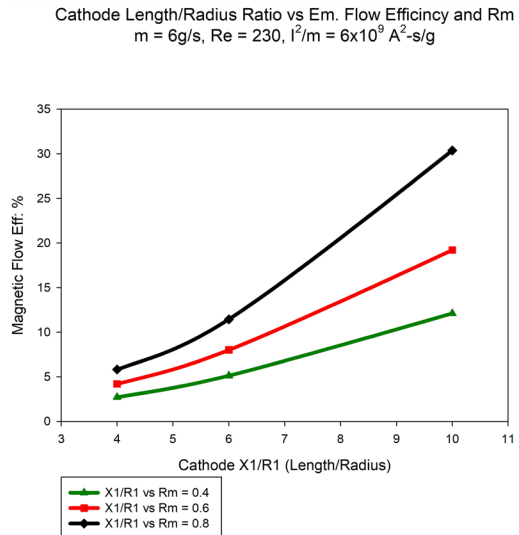

FIGURE 12: FLOW EFFICIENCY VS RM

To understand the rational for the impact of Cathode length ratio on thrust, Figure 13 shows the lateral current density along the length of the Anode at Rm = 0.6. Note that for a longer Cathode there is a higher value of current density (A/m^2) for any location along the Anode surface. Of course, all values are the same at the entry of the MPD thruster and gradually decrease to near zero at the exit plane. The difference is the rate of current density decrease from inlet to exit. Similar results are duplicated at different values of Rm.
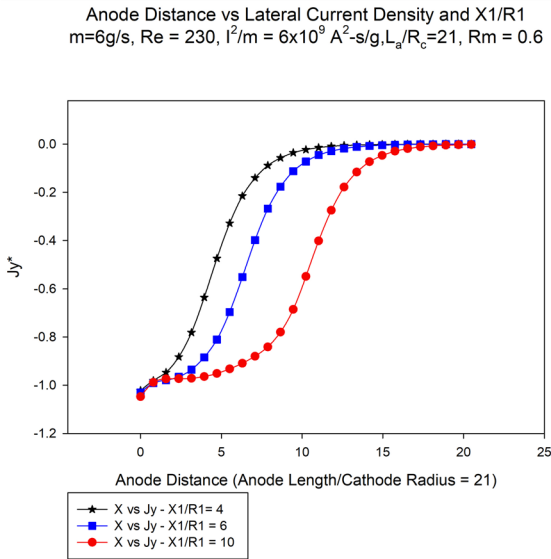
FIGURE 13: ANODE LATERAL CURRENT VS X1/R1

12.1 Heat Transfer Distribution

Figure 14 shows the general temperature distribution for the case of Rm = 0.2, 21,000 Amps, 75x10^9 A^2-s/g, and X1/R1 = 10. The plasma enters at 4,000k and with a 100% ionization, and increases to about 5,572K at the Cathode tip with a Cathode base temperature of 4,400K. Note the slight magnetic cooling at the inlet, the solid Cathode temperature gradients from the base to the Cathode tip, and the temperature cooling along the thruster axis from the Cathode tip to the thruster exit.
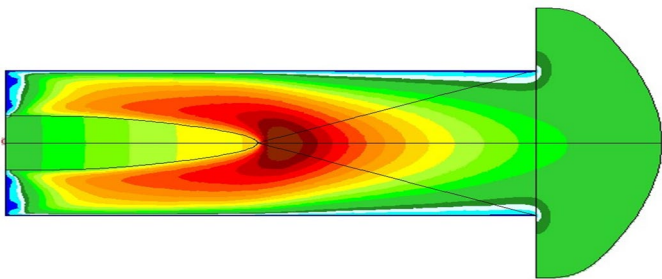

FIGURE 14: BASE TEMPERATURE DISTRIBUTION

Figure 15 shows the variation of velocity, temperature, and

viscosity along the thruster axis, from tip to exit. For this case the temperature as a maximum at the Cathode tip and loses heat to the Anode boundary with a fixed temperature boundary condition equal to the plasma inlet temperature. Along the axis, as the temperature decreases so does the viscosity which is temperature dependent. Thus, a decreasing viscosity results in a decreased viscous diffusion associated with an increased in convective velocity, i.e., acceleration along the axis.
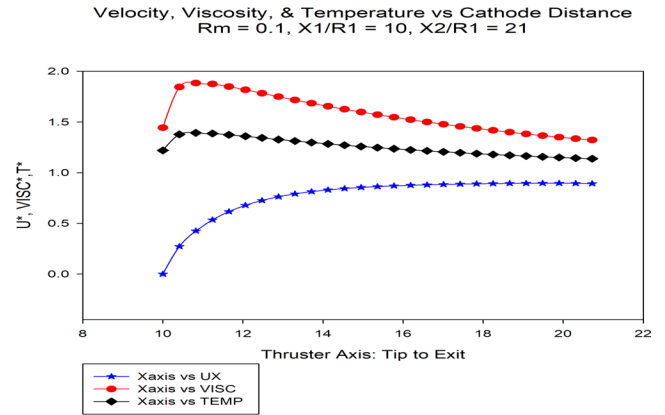

FIGURE 15: AXIAL VELOCITY, TEMPERATURE AND VISCOSITY.

Figure 16 shows the Argon plasma Viscosity-Temperature deployed for the MPD model [1]. Note the inflection at around 10,000K. A design consideration should be a maximum temperature of 10,000K in the vicinity of the Cathode tip, with an expected decrease of temperature and viscosity along the thruster axis. Due to the Argon plasma viscosity variation, the heat transfer from the Cathode to the Anode along the axis will result in thermal acceleration due to reduced viscous diffusion.
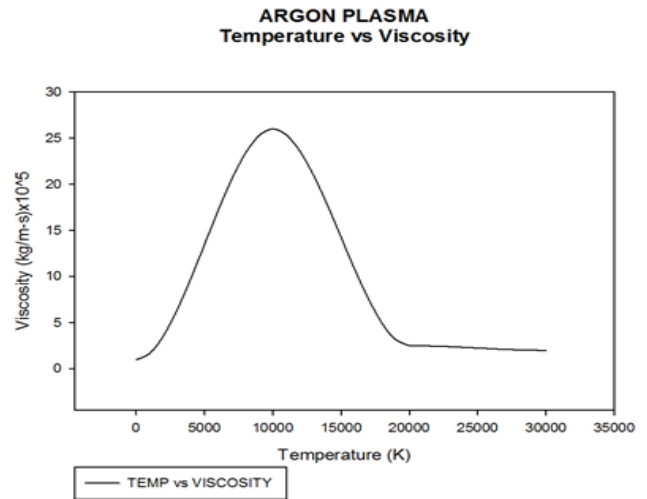

FIGURE 16: ARGON VISCOSITY VS TEMPERATURE

12.2 Anode Heat Flux

The Anode electrode should be maintained at a reduced temperature lower than the Cathode electrode tip to facilitate thruster axial thermal cooling and increased thermal thrust. Figure 17 shows the transverse heat flux along the Anode surface. Note the large heat flux increase a short distance from the plasma inlet.

As the Anode surface temperature has a specified temperature boundary condition the same as the plasma inlet temperature, it is necessary to determine the Anode cooling heat transfer rate based upon the value of Rm and the applied current from the following:
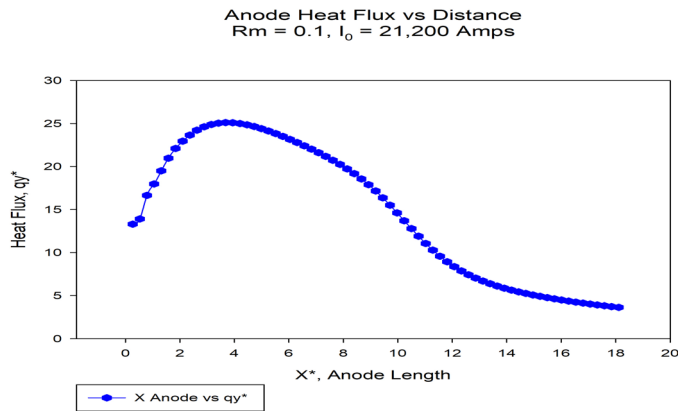

FIGURE 17: ANODE HEAT FLUX VS DISTANCE

$$\overline{q}_y^{"} = \frac{q_0^{"}}{X_2} \int_0^{X_2} q_y^*(x)dx$$

$$q_0^{"} = \frac{\dot{m}cp_0T_0}{A_{cathode}} = \frac{32,592}{A_{cathode}}[\frac{W}{m^2}] \quad (40)$$

For the specified conditions, the Anode heat transfer flux to maintain the Anode wall temperature is $\frac{4,056}{A_{cathode}}\left[\frac{W}{m^2}\right]$. The Anode heat transfer flux varies with Rm, plasma mass flow rate, ionization temperature, geometry, and applied current.

The inclusion of the Cathode solid as a "real" material is necessary to ensure an appropriate heat transfer mechanisms for plasma cooling and temperature management. A large Cathode/plasma thermal conductivity difference contributes to internal heat sinks that balances the plasma heat sources and dampens thermal oscillations leading to stable numerical conversions during the 'modelling' process.

Figure 18 shows the "heat transfer" direction scaled by Temperature values. Note that within an area downstream of the Cathode boundary due to higher plasma temperatures, there is convective heat transfer downstream, heat transfer to the outer Anode boundary due to a lower temperature and to the inner Cathode boundary due to a higher thermal conductivity and a lower temperature. This detail is typically not provided.
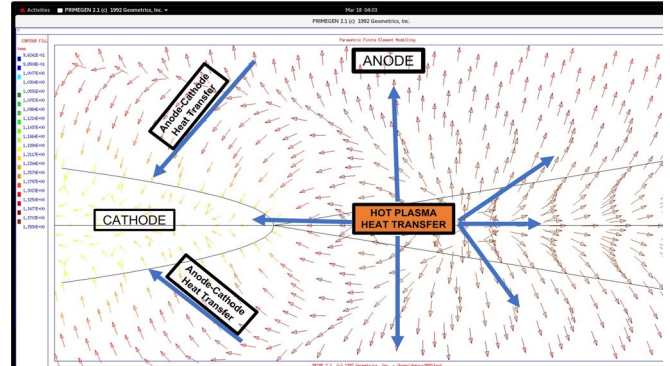

FIGURE 18: PLASMA HEAT TRANSFER VECTORS

This convective/conductive solid/plasma heat transfer process between the plasma fluid and the Cathode solid should be included within the finite element model to capture the interconnectivity between fluid mechanics, heat transfer, and electromagnetics.

13. CATHODE CURRENTS & ENERGY DISSIPATION

Figure 19 shows the Cathode dimensionless axial current distribution $(J_x^* = \frac{1}{Rm}\nabla^* x B^*)$ as a function of the Cathode magnetic Reynolds number. The plasma magnetic Reynolds number is constant at Rm = 0.10. As a "solid" finite element domain element, the relative magnitudes of the magnetic Reynolds number impacts both the axial Cathode current flow and the energy dissipation within that Cathode. Observe that for a Cathode Rmc = 100, the base axial current is higher than a Cathode Rmc = 600. This may not be obvious since a higher Rm indicates a higher electrical conductivity, but also a lower "electrical resistivity".
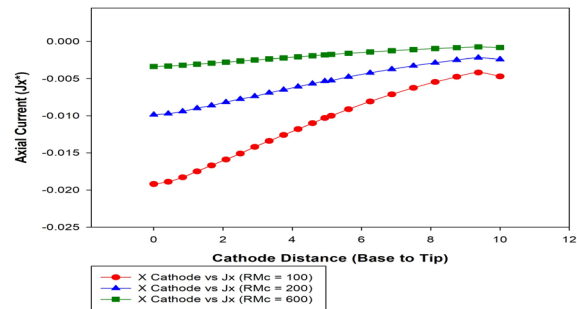

FIGURE 19: AXAL CATHODE CURRENT VS. RM

Note the relatively constant Cathode axial current distribution with increasing values of Rmc (100-600). Numerically, this behavior indicates a computational insensitivity to the ratio of plasma/Cathode magnetic Reynolds number, and we theorize that Cathode materials with a higher electrical conductivity (lower electrical resistivity) also serves to damped plasma fluctuations and improves computational efficiency, i.e., acts as a current 'sink', and provides increased stability.

A higher electrical resistivity (lower Conductivity) results in an increased resistive power deposited into the Cathode, i.e., $\frac{I_0^2}{\sigma}[W]$. Figure 20 shows the Cathode axial resistive power (W/m) (absorption rate) which impacts the resulting Cathode temperature distribution and the heat transfer necessary to maintain the Cathode base surface temperature (T_0). Note that a lower Magnetic Reynolds No. (higher resistivity) results in a higher Cathode energy absorption rate, than a higher Magnetic Reynolds No. (lower resistivity).

Cathode Axial Resistive Power vs Cathode Distance vs Cathode Magnetic Re#
m = 6 gm/s, I = 10,400 A, J0 = 1.95x10^5 A/m^2, T0 = 4,000K, Σ = 583 A/V-m
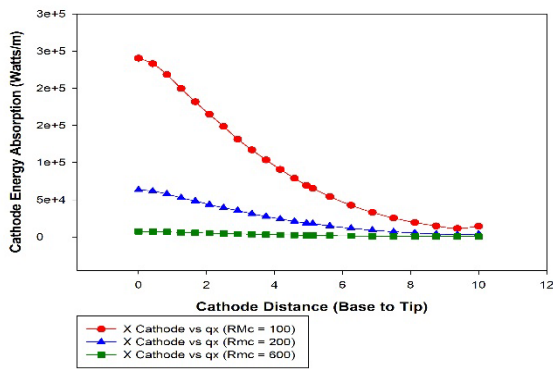

FIGURE 20: CATHODE RESISTIVE POWER VS RM

14. CONCLUSION

The finite element method represents a valuable MPD design tool for comparing multiple geometric variations combined with proper boundary conditions and material properties. The approach herein presented a Conjugate Heat Transfer model for coupling the solid Cathode/Anode elements with the high temperature fluid plasma and combined with the capability to include gradient-based forcing terms and boundary conditions within the finite element stiffness matrix. The completely coupled direct matrix formulation deploys a "wave front" matrix solver operating on a REDHAT LINUX microcomputer with an INTEL P4 Processor.

The dimensionless 2D finite element MPD computational technology methods here provide the foundation for the analysis of both applied and self-field thrusters and is the basis of the CHAOS 2D transient and compressible single temperature plasma code with temperature dependent properties, integrated solid/fluid elements, gradient based loadings and with coupled output variables that include velocity, pressure, temperature, heat flux, and current, electric, and magnetic field density.

The OMEGA design factor, ω, a single variable MPD modeling feature was introduced. This strategy allows the classifying of MPD thrusters based upon variables $\omega(I_0^2, \dot{m}, X_2), Ec, Rm, \dot{m}, and, T_0$.

The model leverages the inherent Galerkin finite element ability to include primary variable gradient-based load terms without difficulty, to naturally include the interface linkage terms from the conservation laws for mass, momentum, energy, and electromagnetics. These interface linkage terms couple the various interdisciplinary computational domains that are inherently gradient based.

Finally, a consideration for the inclusion of solid elements within thermal and magnetic fluid dynamics problems is due to large differences between thermal and electrical conductivity property values. The solid domain represents an energy buffer to absorb random thermal and magnetic flow fluctuations and results in a stable system convergence behavior.

REFERENCES

[1] Berry, K. Joel. "A Two-Dimensional Parametric Computational Framework for Finite Element Heat Transfer Analysis of Self-Field Magnetoplasmadynamic Thrusters", ASME, IMECE2021-72916, 2020.

[2] Parma, Brian J., "Three-Dimensional Modeling and Analysis of Magnetoplasmadynamic Acceleration", Ph.D., Dissertation, Arizona State University, 2011.

[3] Xisto, Carlos M., Pascoa, Jose C., Olivira, Paula J., "Numerical Modeling of a Self-Field Magnetoplasmadynamic Thruster", International Conference on Engineering UBI2013 – 27-29 Nov. 2013, University of Biera Interior, Covilha, Portugal.

[4] Xisto, Carlos M., Pascoa, Jose C., Olivira, Paula J., "Numerical Analysis of Real Gas MHD Flow on Two-Dimensional Self-Field MPD Thrusters", Acta Astronautica, 07/2015, Volume 112.

[5] Hughes, W.F., Young, F. J., The Electromagnetics of Fluids, Wiley & Sons, 1966.

[6] Huebner, K. H., Thornton, E. A., Byron, T. G., The Finite Element for Engineers, Wiley & Sons, 1995.

[7] Sergerlind, L. J., Applied Finite Element Analysis, Wiley & Son, 1976.

[8] LaPointe, M.R., "Numerical Simulation of Self-Field MPD Thrusters", AIAA-91,2341, 1991.

[9] Mayigue, C.C., Groll, R., "Numerical Simulation of Argon Fueled Self-Field Magnetoplasmadynamic Thrusters using the Central-Upwind Scheme Flux Interpolations", European Journal of Mechanics/B Fluids, 72 (2018), 645-663.

[10] Berry, K.J., "An Efficient C Based Wave Front Solver for PC Finite Element Applications, Journal of Mechanical Engineering Systems", Vol. 1, No. 3, 1990.

[11] LaPointe, M.R., "Numerical Simulation of Geometric Scale Effects in Cylindrical Self-self MPD Thrusters", AIAA 92-3297, 1992.

[12] Sovey, J.S., Mantenicks, M.A., "Performance and Lifetime Assessment of MPD Arc Thruster Technology", AIAA 88-3211, 24th JPC July 11-13, 1988.

[13] Myers, R.M., Mantenicks, M.A., Sovey, J.S., "Geometric Effects in Applied-Field MPD Thrusters", AIAA 90-2669, 21st IEPC July 18-20, 1990.

[14] Tahara, H., Yasui, H., Kagaya, Y., Yoshikawa, T., "Experimental and Theoretical Researchers on Arc Structures in a Self-Field Thruster", AIAA 87-1093, 19th IEPC May 11-13, 1987.

[15] Hugel, H., "Effect of Self-Magnetic Forces on the Anode Mechanism of a High Current Discharge", IEEE Transactions on Plasma Science, PS-8(4), December 1980, 437-442.

[16] Lawless, J.L., Subramaniam, V.V., "Theory of Onset in Magnetoplasmadynamic Thrusters", J. Propulsion and Power, 3(2), March-April 1987, 121-127.

[17] Niewood, E., Preble, J., Hastings, D., Martinex-Sanchez, M., "Electrothermal and modified Two Stream Instabilities in MPD Thrusters", AIAA 90-2607, 21st IEPC July 18-20,1990.

[18] Rempfer, D., Auweter-Kurtz, M., Kaeppeler, H.J., Maurer, M., "Investigations of Instabilities in MPD Thruster Flows Using a Linear Dispersion Relation", IEPC 88-071, 20th IEPC October 3-6, 1988.

[19] Nerheim, N.M., Kelley, A.J., "A Critical Review of the State-of-the-Art of the MPD Thruster", AIAA 67-688, AIAA Electric Propulsion and Plasmadynamic Conference, September 11-13, 1967.

[20] Thompson, R.J., Wilson, A., Moller, T., "A Strong Conservative Riemann Solver for the Solution of the Coupled Maxwell and Navier-Stokes Equation", Journal of Computational Physics, Vol. 258, 2014,431-450.

[21] Wagner, H.P., Auweter-Kurtz, M., Roesgen, T., et. al., "Gradient Driven Instabilities in Stationary MPD Thruster Flows", AIAA 90-2603, 21st IEPC July 18020, 1990.

[22] Murphy, A B, et al, "Modeling of Thermal Plasmas for Arc Welding", J. Physics D: Appl. Physics Vol. 42 No. 19, 2009.

[23] Gleizes, A., et al, "Thermal Plasma Modeling", J. Physics D: Appl. Physics, 38, 2005 R153-R183.

[24] Chandrupatla, T.R. Belegundu, A. D., Introductions to Finite Elements in Engineering, Prentice Hall, 1991.

[25] Lewis, R.W.,Morgan, K.,Thomas, H.R., Seetharamu, K.N., The Finite Element Method in Heat Transfer Analysis, Wiley & Sons, 1996.

[26] Chelem, C., Groll, R., "Magneto-Plasmadynamic Thruster Modeling with Coaxial Induced Magnetic Field", Int. J. Comp. Meth and Exp. Meas., Vol. 4, No. 4, 2016, 380-392.

[27] ntrs.nasa.gov/archive/nasa/casi.ntrs.nasa.gov/20070032050.pdf

[28] D. Giordano, in: 33rd Plasmadynamics and Lasers Conference, Fluid Dynamics and Co-located Conferences, American Institute of Aeronautics and Astronautics, 2002.

[29] D. Li, C. Merkle, W.M. Scott, D. Keefer, T. Moeller, R. Rhodes, "Hyperbolic Algorithm for Coupled Plasma/Electromagnetic Fields Including Conduction and Displacement Currents", AIAA J. 49 (2011) 909–920.

[30] J. Picone, R. Dahlburg, "Evolution of The Orszag-Tang Vortex System In A Compressible Medium 11. Supersonic Flow", Phys. Fluids, B Plasma Phys. 3 (1991) 29–44.

[30] Sankaran, K. "Simulation of MPD Flows Using A Flux-Limited Numerical Method For The MHD Equations", Ph.D. Thesis, Princeton University, Technology and Medicine, Princeton, 2005.

[31] Ahagar, M., Ebrahimi, R., Shams, M., "Numerical Simulation of no-equilibrium Plasma Flow in a Cylindrical MPD Thruster Using a High-Order Flux-Difference Splitting Method". Act Astronaut, 103 (2014) 129-141.

[32] Kumar, Mahendhran M, and Amit, "Numerical Study on Self-Field Two-Dimensional Straight Anode MPD Thruster", Internal Journal of Aerospace Innovations, Volume 3, No. 4, 2011.